Dynamics of dense gravity currents and mixing in an up-sloping and converging vee-shaped channel

Dynamics of dense gravity currents and mixing in an up-sloping and converging vee-shaped channel

JANEK LAANEARU (IAHR Member), Associate Professor, *Department of Mechanics, Tallinn University of Technology, Tallinn, Estonia*
Email: janek.laanearu@ttu.ee (author for correspondence)

ALAN J. S. CUTHBERTSON (IAHR Member), Lecturer, *Institute of Infrastructure and Environment, Heriot-Watt University, Edinburgh, UK*
Email: a.cuthbertson@hw.ac.uk

PETER A. DAVIES (IAHR Member), Professor, *Department of Civil Engineering, University of Dundee, Dundee, UK*
Email: p.a.davies@dundee.ac.uk

Dynamics of dense gravity currents and mixing in an up-sloping and converging vee-shaped channel

ABSTRACT

Detailed velocity and density measurements are used to investigate dense water dynamics in an inclined, silled channel of triangular cross-section with varying side slope α and adverse bed slope ϕ. For the steeper channel configuration considered ($\phi = 3.6°$), the dense-water bottom current is shown to be frictionally-controlled, with an internal flow structure characterised by a sharp pycnocline and decreasing isopycnal separation in the along-channel direction. For the milder up-sloping channel ($\phi = 1.7°$), the dense water outflow is shown to be hydraulically-controlled as the channel sill section is approached, with internal flow dynamics characterised by increasing isopycnal separation in the along-channel direction. Analysis of the gradient Richardson number Ri_g of the flow confirms that hydraulically-controlled flows dilute the active bottom water due to interfacial mixing. A gradually-varying internal flow model and a two-layer hydraulic modelling approach are shown, respectively, to represent adequately the outflow behaviour for these two bed slope conditions.

Keywords: Stratified flows and density currents, Buoyancy-driven flows, Hydraulic models, Laboratory studies, Froude number, Richardson number, Reynolds number

1 Introduction

Topographic constraints on water passage are important in many environmental hydraulics problems such as salt water intrusion into estuaries and tidal inlets (Jackson *et al*. 2008), water exchange within fjordic basins (Fristedt *et al*. 2005) and, on the larger scale, deep-water transport in oceanic straits (e.g. Borenäs and Lundberg 1988, Laanearu and Lundberg 2003, Davies *et al*. 2006). For such problems, the influence upon the flow of the Earth's rotation is important to a greater or lesser degree, depending essentially upon the ratio of the internal Rossby radius of deformation to the width of the topographically controlled region. In cases where this ratio is greater than unity and rotation effects do not control the flow, a two-layer flow hydraulics approach is justified to deal with stratified flow dynamics (e.g. Baines 1984, Armi 1986, Armi and Farmer 1986, Farmer and Armi 1986). These models generally neglect the effects upon the internal flow dynamics of mixing between the two water layers. In narrow straits and estuaries where water masses from different sources meet, boundary friction effects on internal flow dynamics can become important when the channel length (L) to depth (H) ratio L/H becomes large [$L/H > O(10^3)$, Pratt (1986)], while the roles of density stratification and interfacial shear are also important in stratified flow mixing (e.g. Osborn 1980, Ivey and Imberger 1991, Lorke *et al*. 2005). In this regard, many experimental (e.g. Zhu and Lawrence 2000, Cuthbertson *et al.* 2004) and theoretical studies (e.g. Schijf and

Schönfeld 1953, Arita and Jirka 1987a, Stenström 2003) have considered internal energy losses due to bottom friction and interfacial shear in such two-layer channel flows. In addition, attempts to generalise hydraulic theory to account for bottom friction and interfacial mixing (e.g. Ivey 2004, Hogg *et al*. 2006) have, for example, demonstrated the importance of the complex interplay between aspect ratio, horizontal density differences and depth-integrated vertical diffusivity. In the inviscid case (Dalziel 1991, 1992), a dense water layer entering a narrow, silled channel from an upstream basin will become internally critical (or hydraulically-controlled), a flow configuration corresponding well to frictionless, open-channel weir flow hydraulics. However, the effects of boundary friction and interfacial shear may be expected to change this gravity current propagation and the critical flow conditions developed in the presence of a submerged sill. In addition, the question as to how the channel bottom slope will affect dense water transport and internal flow dynamics within a propagating gravity current remains an interesting problem that is not well understood for topographically-constrained, buoyancy-driven, intrusive flows. The cumulative effect of this type of two-layer flow is that diffusive mixing occurs across the pycnocline between the intruding bottom saline water and the overlying fresh or brackish water (e.g. with a net increase in salinity within the outflowing upper layer, Arita and Jirka (1987b)).

The effect of channel cross-sectional shape has been noted as being crucial to the dynamics of hydraulically-driven exchange flows. Previous studies (e.g. Pratt and Whitehead 2007) have applied models formulated on the solution of the general equation for gradually-varied flow in the reduced-gravity limit to predict the effects of boundary friction on longitudinal interface profiles generated along rectangular channels. Laanearu and Davies (2007) extended this reduced gravity hydraulic modelling approach to simulate stratified, internal flows in so-called quadratic cross-section, natural channels. Laanearu *et al*. (2011) demonstrated how this internal hydraulic theory can be applied to a quadratic channel to predict stratified, bi-directional fluxes and observed density interface elevations within a river estuary of the Baltic Sea.

In the case of a uni-directional gravity current propagating in a non-rectangular, non-rotating channel, a single hydraulic control between sub-critical and super-critical outflow conditions is possible at some topographic constriction (e.g. a constraint in channel width or a submerged sill), if boundary and interfacial frictional effects on the stratified flow are comparatively small. However, in situations where frictional effects dominate, the reduced gravity flow cannot adjust to this hydraulically-controlled condition, remaining sub-critical throughout the channel. In this latter case, the hydraulically-driven stratified flow is classified as being frictionally-controlled (e.g. Pratt 1986).

In the current study, detailed experimental measurements are presented for the development of gravity currents along a converging, vee-shaped channel, for two separate

adverse bed slope cases. The main aim of this study is to quantify the relative importance of boundary friction and interfacial processes for the flow development, in order to provide improved insight into the internal flow dynamics associated with stratified flow mixing and the influence of bed topography. In this regard, understanding the dynamical effects due to interfacial mixing is important for many coastal-engineering applications related to salt wedge conditions (e.g. Sargent and Jirka 1987) and tidally-induced salt water intrusions into estuaries and tidal inlets (e.g. Cuthbertson *et al*. 2006). The specific two-layer configuration modelled herein is particularly relevant to estuarine and fjordic exchange flows with reduced upper layer motion (Laanearu *et al*. 2007). Similarly, the presence of natural topographic flow obstructions (e.g. sandbars, submerged sills) determine the water and nutrient exchanges in both tidal and non-tidal inlets (Cuthbertson *et al*. 2006), and can thus have significant implications for the intrusion of saline marine waters into semi-enclosed estuarine impoundments, regional seas and fjords. In this sense, the topographical effects on dense water outflows resulting from adverse bed slope and imposed sill conditions in non-rectangular channels determine the degree to which estuaries and fjords experience larger cumulative effects from interfacial entrainment and mixing than others (Farmer and Armi 1999).

2 Experimental Arrangement

The topographic system under investigation consists of an upstream entry basin, a converging channel and an exit sill section, as shown schematically in Fig. 1, with the main channel dimensions and side wall angles $\theta(y)$ (= $\tan^{-1}\alpha$) also defined. The Cartesian coordinate frame (x,y,z) is orientated with x- and y-axis in the cross- and along-channel directions, respectively and the z-axis is anti-parallel to the gravitational acceleration vector g = (0,0,–g). Measurement locations within the channel are defined relative to reference points x = 0 and y = 0, located along the channel centreline [i.e. axis CC', Fig. 1b] and across the exit sill from the converging channel section [i.e. section 6, Fig. 1b], respectively. The datum elevation (i.e. z = 0) is defined by the lowest in-channel bed elevation (see Fig. 2). Two adverse bottom configurations (i.e. ϕ = 3.6° and 1.7°) were investigated, as sketched in Fig. 2. The maximum in-channel water depth was H_{max} = 334 mm in both cases, while the bed elevation at the end of the converging channel (i.e. sill section 6) was z_s = 114 mm and 53.5 mm, respectively, for the ϕ = 3.6° and 1.7° cases.

Prior to each experiment, the converging channel topography was installed within a large 0.5 m-deep, circular tank filled to a total depth H = 440 mm with freshwater of density ρ_0 = 998.5 kg m^{-3}, fully submerging the topographic channel. Brine solution of density ρ_1 = 1011.4 kg m^{-3} was pumped into the upstream end of the basin via a dispersed source manifold

[see Fig. 1b] with initial flow rate Q_1 = 0.3 l s^{-1}. The reduced gravitational acceleration for this dense water source inflow was $g'_0 = g(1 - \rho_0/\rho_1)$ = 0.125 m s^{-2}. In order to maximise the parametric conditions tested, the brine volume influx was increased in discrete stages to Q_1 = 0.6 l s^{-1} and 0.9 l s^{-1} at prescribed times during each experimental run. After each flow rate increase, the dense water layer adjusted to a new quasi-equilibrium outflow condition for the specified Q_1 value. The resulting steady-state dense bottom gravity current propagated along the converging channel, remaining fully-contained within the submerged channel topography along its full length, before spilling out freely from the uniform-width exit channel section [i.e. downstream of sill section 6, Fig. 1b].

The internal flow dynamics for a constant salt water influx into the submerged topography can be characterised in terms of the channel Reynolds number R_{c1} and Froude number F_1 for the dense bottom water outflow along the triangular channel. Here, $R_{c1} = v_1 R_1/\nu$, where v_1 is the mean dense water layer velocity, ν is the kinematic viscosity and R_1 is the hydraulic radius specified for the dense outflow layer constrained by the triangular bottom boundary and interface [where $R_1 = A_1/\chi_1$, with flow area $A_1 = h_1^2/\alpha$, the total wetted perimeter $\chi_1 = 2h_1\left(\sqrt{1+(1/\alpha^2)}+(1/\alpha)\right)$, and h_1 defined as the centreline (maximum) depth of the bottom outflow layer]. For the current experiments, the bottom boundary related R_{c1} varied between 400 and 2800 within the converging, up-sloping channel between sections 4 and 6 [Fig. 1b]. The densimetric Froude number is defined as $F_1^2 = 2v_1^2/(g'h_1)$, from which the hydraulic depth of the dense water layer is defined by $h_1/2$. Estimated F_1 values within the converging channel indicate that the gravity currents are subcritical ($F_1^2 < 0.016$ for both bed slope cases) at section 4 (Fig. 1) and remains subcritical ($F_1^2 < 0.47$) for $\phi = 3.6°$ cases at sill section 6. By contrast, critical flow conditions ($F_1^2 \rightarrow 1.0$) occur only at sill section 6 for $\phi = 1.7°$ runs.

2.1. *Experimental Instrumentation*

Three-component (u,v,w) velocity measurements for each outflow condition were obtained using a Nortek AS Vectrino acoustic Doppler velocimeter (ADV). The ADV probe was mounted on a traversing system to measure depthwise velocity profiles at five cross-channel locations (i.e. x = –10, –5, 0, 5, 10 cm) across the outflow width in the channel exit section (y = 5 cm downstream of Section 6, Figs. 1 and 2). The measurement frequency of the ADV was set at 10 Hz with the traversing system operating at a constant vertical speed 5 mm s^{-1}.

Full-depth density profiles $\rho(z)$ were obtained as fixed positions within the basin and converging-channel using an array of high-resolution micro-conductivity probes (Cuthbertson *et al*. 2011). The probes were mounted on rigid support frames, each with a motorised rack system that allowed simultaneous and rapid vertical profiling of the density field at these

locations. A total of 100 profiles were obtained for each brine inflow condition at a temporal resolution of 10 seconds between profiles. In the ϕ = 3.6° case, density profiles were measured at three cross-channel locations at both section 4 (i.e. x = –10, 0, 10 cm; y = –75 cm) and adjacent to section 6 (i.e. x = –5, 0, 5 cm; y = –2.3 cm) [see Figs. 1 and 2a]. For the ϕ = 1.7° case, density profiles were measured at 7 locations along the channel centreline [i.e. x = 0 cm; y = –6.5, –21.5, –36.5, –56.5, –76.5, –178.5, –190.5 cm; Fig. 2b].

Vertical variations in density $\rho(z)$ and along-channel velocity component $v(z)$ were analysed by fitting high-order spline curves to individual profiles (see Fig. 3). In general, this smoothing procedure allows for improved characterisation of parameters that are related to time-averaged velocity and density gradients (e.g. buoyancy frequency, shear and the gradient Richardson number).

3 Experimental Results

The dense water flow through the topographic system may be divided into three regions: (i) an inlet region at the upstream end of the basin; (ii) a gradually-varying flow region along the basin and converging-channel sections; and (iii) an outlet region along the uniform exit channel. Although the inflow volume flux Q_1 is increased incrementally during the experiment, the results presented herein consider only quasi-equilibrium conditions within the gradually-varying flow region, once a steady dense water outflow has become fully established for each inflow condition.

3.1. *Quantitative Observations*

In Fig. 4, the fitted density profiles for probes P1 and P4 in the ϕ = 1.7° and 3.6° runs, respectively, are shown for different volumetric inflow rates Q_1. Each steady-state profile is derived only from the temporal average of the last 20 density profiles taken prior to each increase in Q_1. The observed stratification within the converging channel section shows distinct variations between the two bed slope cases. Specifically, density profiles obtained in the ϕ = 3.6° case reveal sharper pycnoclines between the outflowing dense water and overlying fresh water layers, compared with the ϕ = 1.7° case.

Similarly, in Fig. 5, the corresponding spline fits to ADV-measured along-channel velocity (v) profiles are shown for both ϕ = 3.6° and 1.7° runs under different volumetric inflow rates Q_1. As velocity measurements were taken during both the descending and ascending ADV probe excursions, the velocity profiles plotted are averaged over these two excursions. The measured cross-channel and vertical velocity components (u,w) were noted as being small (with zero mean) within the bottom water outflowing layer, while the along-

channel velocity profiles presented (Fig. 5) also indicate that the overlying ambient water layer remains largely quiescent for all cases. Direct comparison between Fig. 5a and 5b highlights the significant influence that the bed slope and sill condition has on the magnitude of the core velocity within the outflowing bottom layer. In particular, for the largest volumetric inflow $Q_1 = 0.9$ l s^{-1}, the measured core velocity $v_{max} \rightarrow 0.05$ m s^{-1} for the $\phi = 3.6°$ case is considerably lower than that associated with the corresponding outflow for $\phi = 1.7°$, where $v_{max} \rightarrow 0.08$ m s^{-1}.

In Fig. 6, combined plots of normalised density excess $\rho'(z)$ [= $(\rho-\rho_0)/(\rho_1-\rho_0)$] and non-dimensional velocity $v(z)/v_{max}$ profiles adjacent to sill section 6 are compared for the dense water inflow $Q_1 = 0.9$ l s^{-1} runs, as well as indicating the relative positions of peak density (dρ/dz) and velocity (dv/dz) gradients. Fig. 7 plots corresponding density excess $\rho'(z)$ and density gradient dρ/dz profiles at different locations along the converging channel for the $Q_1 = 0.9$ l s^{-1} runs. For the $\phi = 3.6°$ case [Figs. 6a and 7a], the density interface height, defined nominally by the elevation of the $\rho' = 0.5$ isopycnal, is shown to coincide closely with the elevation of the peak density gradient (dρ/dz); a characteristic found under all inflow Q_1 conditions and at different channel locations [Fig. 7a]. With a similar definition given to the velocity interface, $v(z)/v_{max} = 0.5$ (i.e. 50% of the dense water layer core velocity), the relative velocity magnitude associated with peak velocity gradient (dv/dz) is also found to correspond to $v/v_{max} \approx 0.5$ [i.e. coinciding at $(z - z_b)/H \approx 0.47$ close to sill section 6, Fig. 6a]. By contrast, for the $\phi = 1.7°$ case [Fig. 6b and 7b], although the normalised density and velocity interfaces ($\rho' = v/v_{max} = 0.5$) coincide [at $(z - z_b)/H \approx 0.31$, Fig. 6b], the peak density (dρ/dz) and velocity (dv/dz) gradients are shown to correspond to $\rho' = 0.28$ [at $(z - z_b)/H \approx 0.33$, Fig. 6b] and $v/v_{max} = 0.55$ [at $(z - z_b)/H \approx 0.31$, Fig. 6b], respectively. This demonstrates differences in the internal flow structure for the two slope conditions.

The lower layer critical depth $h_{c1} = 2v_1^2/g'$ [with $v_1 \approx Q_1\alpha/h_{c1}^2$] was calculated at sill section 6 to be 8.86 cm for $Q_1 = 0.9$ l s^{-1} and $\alpha = 0.649$ ($\theta = 33°$). This corresponds to non-dimensional values $h_{c1}/H = 0.402$ and 0.316 for the $\phi = 3.6°$ and 1.7° runs, respectively, indicating that dense water outflows are generally subcritical along the converging channel [i.e. lower layer thickness $(z_{(\rho'=0.5)} - z_b)/H > h_{c1}/H$]. Critical conditions are only achieved at sill section 6 for the milder slope case. It is noted that similar differences in the internal structure of the dense bottom gravity currents are observed at all Q_1 values.

Longitudinal variations in stratification are obtained from spline-fitted density excess $\rho'(z)$ and gradient ($d\rho/dz$) profiles at the channel centreline for the $\phi = 3.6°$ [i.e. P1 and P2; Fig. 7a] and $\phi = 1.7°$ [i.e. P3, P4, P5 and P6; Fig. 7b] cases. It is apparent from Figs. 7a and 7b that the along-channel variation in pycnocline thickness and peak density gradient are

different for the two bed slopes conditions. For the ϕ = 3.6° case, a sharper interface and higher peak density gradient suggests that the isopycnals converge in the downstream direction [Figs. 2a and 7a]. By contrast, for the ϕ = 1.7° case, a more diffuse interface with reducing peak density gradients suggest that the isopycnals diverge in the downstream direction [Figs. 2b and 7b]. A measure of the pycnocline thickness Δh, estimated as the elevation difference of the ρ' = 0.4 and 0.6 isopycnals, can be used to demonstrate this behaviour. For example, the change in pycnocline thickness along the converging channel between cross-sections 4 and 6 [Fig. 1(b)] can be estimated from the density data plotted in Figs. 7a and 7b (i.e. for Q_1 = 0.9 l s^{-1} runs). These normalised pycnocline thicknesses vary between $\Delta h/H_{max} = 4.8\times10^{-3} \rightarrow 2.1\times10^{-3}$ for the ϕ = 3.6° case [Fig. 7a] and $\Delta h/H_{max} = 1.9\times10^{-2} \rightarrow 2.5\times10^{-2}$ for the ϕ = 1.7° case [Fig. 7b]. Qualitatively similar pycnocline behaviour is observed at other Q_1 values.

4 Reduced Gravity Hydraulic Model

In order to model the observed behaviour of the dense bottom water layer along the converging and up-sloping, triangular channel, a reduced-gravity hydraulic modelling approach is first applied. Steady internal flow behaviour in the along-channel y direction is governed by the following momentum and continuity equations, derived for the triangular channel configuration:

$$v_1 \frac{\mathrm{d}v_1}{\mathrm{d}y} + g' \frac{\mathrm{d}h_1}{\mathrm{d}y} = -g' \frac{\mathrm{d}z_b}{\mathrm{d}y} - C_b \frac{v_1^2}{R_{1,b}} - C_i \frac{v_1^2}{R_{1,i}}, \tag{1}$$

$$h_1^2 \frac{\mathrm{d}v_1}{\mathrm{d}y} + v_1 \frac{\mathrm{d}}{\mathrm{d}y}\left(h_1^2\right) = \frac{v_1 h_1^2}{\alpha} \frac{\mathrm{d}\alpha}{\mathrm{d}y}, \tag{2}$$

where v_1 is the mean velocity in the lower layer, $R_{1,b} = h_1/(2\sqrt{\alpha^2+1})$ is the hydraulic radius associated with the channel boundary, and $R_{1,i} = h_1/2$ is the hydraulic radius due to the interface (i.e. equivalent to the hydraulic depth for the triangular channel). In the converging channel (between sections 2 and 6, Fig. 1), a coefficient $\sqrt{\alpha^2+1} \approx 1$ [i.e. θ = 18.4° – 33°, Fig. 1a], and, therefore, $R_{1,b} \approx R_{1,i}$. The total drag coefficient C_f ($\approx C_b + C_i$), representing the quadratic friction law, is used to estimate internal dissipation along the channel due to bottom boundary friction (through $C_b = f/8$, where f is the Darcy-Weisbach friction factor) and interfacial drag (through C_i). Under steady conditions the gradually-varying dense water outflow, due to variations in bottom height $z_b(y)$ and cross-sectional side slope $\alpha(y)$, is determined by the balance between inertial, buoyancy and shear forces. Thus, an equation to predict the gradually-varying bottom layer thickness $h_1(y)$, accounting for both geometric

variations and friction effects, can be derived by combining Eqs. (1) and (2) and substituting for Froude number $\mathrm{F}_1^2 = 2v_1^2/(g'h_1)$:

$$\frac{\mathrm{d}h_1}{\mathrm{d}y} = \frac{\dfrac{\mathrm{d}z_b}{\mathrm{d}y} + \dfrac{h_1}{2\alpha}\mathrm{F}_1^2\dfrac{\mathrm{d}\alpha}{\mathrm{d}y} + C_f\mathrm{F}_1^2}{\mathrm{F}_1^2 - 1}. \qquad (3)$$

Eq. (3) can be solved numerically for $h_1(y)$ with specified initial conditions upstream (i.e. Q_1, g', h_1). In a study of hydraulically-driven reduced gravity flows in a uniform-width, silled rectangular channel, Pratt (1986) specified that the conditions required for critical flow (i.e. $v_1^2 = g'h_1$), and the location of the control section, were dependent primarily on the friction coefficient C_f. For inviscid flow conditions (i.e. $C_f = 0$), critical flow was shown to form at the channel sill section, whilst, with the inclusion of frictional effects (i.e. $C_f > 0$), the control section formed at a location where the along-channel bed slope $-\mathrm{d}z_b/\mathrm{d}y = C_f$. Similarly, for cases in which $C_f > -\mathrm{d}z_b/\mathrm{d}y$, the flow did not adjust to critical flow conditions, remaining subcritical throughout (a condition referred to as frictionally-controlled flow).

For the triangular channel configuration presented here (Fig. 1), the dense bottom water layer thickness h_1 cannot be treated independently from the interface width w_1, since $h_1 = \alpha w_1/2$. Thus, the layer thickness h_1 corresponding to critical flow conditions ($\mathrm{F}_1^2 = 1$) is derived from Eq. (3) as:

$$\left(\frac{\mathrm{d}z_b}{\mathrm{d}y}\right)_{y=y_{c1}} + \left(\frac{h_1}{2\alpha}\frac{\mathrm{d}\alpha}{\mathrm{d}y}\right)_{y=y_{c1}} = -C_f \qquad (4)$$

where y_{c1} is the along-channel location at which the hydraulic control is formed. According to Eq. (4), critical flow conditions cannot occur within the converging, up-sloping channel of the current experimental system, as $\mathrm{d}z_b/\mathrm{d}y > 0$ and $\mathrm{d}\alpha/\mathrm{d}y > 0$. Moreover, considering the uniform-width ($\mathrm{d}\alpha/\mathrm{d}y = 0$) exit channel beyond sill section 6, it is noted that the along-channel slope is different for the two bed configurations tested ($\mathrm{d}z_b/\mathrm{d}y = 0.0$ and -0.027 for $\phi = 3.6°$ and 1.7°, respectively, see Fig. 2). Thus, for frictional flow conditions ($C_f > 0$), the control section will not form in the horizontal exit channel for the $\phi = 3.6°$ runs, with the bottom outflow remaining subcritical along the full channel length. By contrast, a hydraulic control may be expected to form in the down-sloping exit channel for the $\phi = 1.7°$ case, which, according to Eq. (4), will occur at a channel location where the local bed slope satisfies the condition $-\mathrm{d}z_b/\mathrm{d}y = C_f$.

The hydraulically-driven flow solutions to Eq. (3) are presented in Fig. 8 for the $\phi = 3.6°$ runs along the 0.5 m converging channel section immediately upstream of sill section 6. Under inviscid flow conditions ($C_f = 0$; represented by solid curves in Fig. 8), with specified

upstream conditions (Q_1, g', h_1), the along-channel interface predictions are shown to converge to a control section ($F_1^2 = 1$) exactly at sill section 6 [i.e. where $d\alpha/dy = dz_b/dy = 0$ for $C_f = 0$ in Eqs. (3) and (4)]. However, when frictional effects are included [e.g. $C_f = 0.025$, for otherwise identical upstream conditions (Q_1, g', h_1) to the inviscid case], the theoretical solutions (dashed curves in Fig. 8) reveal the formation of a branch point between subcritical ($F_1 < 1$) and super-critical ($F_1 > 1$) solutions located upstream of sill section 6. This branch point represents a "frictionally-induced singularity", which has mathematical significance in the reduced gravity flow problem (Laanearu and Lundberg 2005). It arises as the specific energy E_1 [$= v_1^2/(2g') + h_1 + z_b$] in the reduced gravity limit is no longer conserved along the channel, and thus for a conserved flux ($dQ_1/dy = 0$), the specified upstream depth h_1 is now insufficient to account for this energy dissipation. As a consequence, the hydraulic model fails to generate continuous, hydraulically-driven flow solutions along the full converging channel and no real solutions are possible at locations downstream of this critical branch point ($F_1 = 1$). [It should be noted that as frictional dissipation of energy is even more pronounced in the $\phi = 1.7°$ case, the singularity will be located further upstream in the channel.] Thus, in order to attain continuous interface predictions for frictional runs, the upstream specific energy function E_1 must be adjusted (through increasing h_1) to account for this energy dissipation (see dot-dash curves in Fig. 8).

Fig. 9 compares theoretical reduced gravity solutions with measured $\rho' = 0.5$ density interface elevations for runs conducted under both bed slope conditions. For the $\phi = 3.6°$ runs [Fig. 9a], the dense bottom gravity current is shown to remain subcritical along the converging channel, as measured interface elevations lie above the corresponding inviscid flow solutions [solid curves in Fig 9a]. Improved fit to the experimental data is achieved through the computation of frictional flow solutions ($C_f \approx C_b + C_i > 0$) and specification of an increased upstream specific energy E_1 condition (through increased h_1) [dashed curves in Fig. 9a] to ensure continuous flow solutions are generated. In this regard, the acceleration of the bottom gravity current towards the sill indicates that the bottom friction coefficient $C_b = f/8$ will reduce in the longitudinal direction [e.g. $f = 0.3164(4R_{c1})^{-1/4}$, Blasius equation], while the interfacial drag coefficient C_i is set constant (= 0.0255) along the channel. Corresponding inviscid and frictional flow solutions for the $\phi = 1.7°$ runs [solid and dashed curves in Fig. 9b] are, by contrast, shown to provide relatively poor representation of the measured interface elevations. This discrepancy is an indication of interfacial mixing within these $\phi = 1.7°$ runs.

In order to determine the energy dissipation (i.e. dE_1/dy) along the converging channel, the specific energy function E_1 can be used to derive a weir-type relationship for so-called maximal flow conditions (i.e. $dE_1/dh_1 = 0$, leading to $F_1 = 1$):

$$Q_1 = C_d \; g'^{1/2} \left(\frac{2}{5} \Delta z \right)^{5/2} \frac{4}{\alpha} . \qquad (5)$$

Here, C_d is a discharge coefficient accounting for the total internal head loss ΔE_I due to frictional drag along the converging channel and $\Delta z = (h_{1,\max} - z_s)$ is the maximum bottom water layer height above the minimum bed elevation $z_b = z_s$ at sill section 6 (see Fig. 2). Eq. (5) can therefore be used to determine appropriate discharge coefficients C_d corresponding to the gradually-varied flow solutions [Eq. (3)] for different frictional conditions [where clearly $C_d = 1$ for inviscid flow conditions ($C_f = 0$)]. As an example, when $C_f = 0.025$ is specified in the reduced gravity flow model, a corresponding discharge coefficient $C_d = 0.92$ is obtained for volumetric fluxes $Q_1 = 0.3$, 0.6 and 0.9 l.s^{-1}. Thus, the specific energy functions E_1 at the entrance and sill sections of the converging channel (sections 2 and 6, respectively, Fig. 1) can be used to determine the internal head loss $\Delta E_{I(2)\rightarrow(6)}$ (> 0) for known Q_1 values and calculated C_d (< 1) values using Eq. (5). In such hydraulically-driven internal flows, this energy dissipation may be predominantly due to an upward cascade of energy toward the ambient upper layer due to friction and interfacial mixing processes (i.e. net entrainment through the pycnocline). This latter effect, in stratified two-layer systems, is known also as interface ″ventilation″ (Kõuts and Omstedt 1993).

5 Two-Layer Hydraulic Model

The failure of the single-layer reduced gravity model to adequately predict dense water outflows obtained during the $\phi = 1.7°$ runs is mainly associated with considerable energy dissipation due to strong interfacial mixing processes. To investigate the effects of stratification and internal flow structure within this case, a two-layer hydraulic model (Dalziel 1992) has been modified to simulate the current experimental configuration. According to Laanearu and Davies (2007), the non-dimensional internal energy equation, representing the difference between the lower (B_1) and upper-layer (B_0) Bernoulli functions [i.e. $K_i = (B_1 - B_0)/g'$] for small density variations between the two layers [i.e. $(1 - \rho_0/\rho_1) << 1$] and the vee-shaped channel configuration is given by:

$$K_i^* = 4 \, K_{ii}^* \left(\left(\frac{1}{h_1^*} \right)^4 - \frac{q^2}{\left((H^*)^2 - (h_1^*)^2 \right)^2} \right) + h_1^* + z_b^* \qquad (6)$$

where the dimensionless parameters are the internal head $K_i^* = K_i / H_{\max}$, a lower layer volume flux parameter $K_{ii}^* = Q_1^2 \alpha^2 / (8 g' H_{\max}^5)$, the local water depth $H^* = H/H_{\max}$, the lower layer height $h_1^* = h_1/H_{\max}$ and the bottom bed height $z_b^* = z_b/H_{\max}$. The ratio of the upper and lower layer volume fluxes is represented by $q^2 = Q_0^2/Q_1^2$. Eq. (6) can be used to specify the non-

dimensional internal head loss along the converging channel section [i.e. $\Delta E^*_{I\,(2)\rightarrow(6)} = K^*_{i\,(2)} - K^*_{i\,(6)}$ (e.g. Zhu and Lawrence 2000). Solutions for this two-layer flow model [Eq. (6)] can be parameterized by a composite Froude number $\mathsf{G}^2 = \mathsf{F}_0^2 + \mathsf{F}_1^2$, where $\mathsf{F}_0^2 = 2v_0^2 h_1/[g'(H^2 - h_1^2)]$ is the densimetric Froude number of the upper layer and F_1^2 is as defined previously. In order to utilise the two-layer model [Eq. (6)] for direct comparison with the reduced gravity hydraulic model [Eq. (3)], the upper layer must therefore be specified as inactive (i.e. Q_0, v_0, $\mathsf{F}_0^2 \rightarrow 0$). The specific condition of an inviscid dense bottom water current [i.e. $C_f = 0$ in Eq. (3)] thus corresponds to the two-layer hydraulic model predictions [Eq. (6)] with no change in internal head along the converging channel (i.e. $\Delta E^*_{I\,(2)\rightarrow(6)} = 0$).

To quantify the relative importance of energy dissipation due to interfacial mixing within the two channel topographies, bed friction effects are first considered, in isolation, by running the reduced gravity model [Eq. (3)] with $C_f = C_b = f/8$ along the converging channel and critical conditions ($\mathsf{F}_1^2 = 1$) imposed at sill section 6. For all runs ($\phi = 3.6°$ and 1.7°), the calculated bottom drag coefficients range within 7.2×10^{-3} (at section 2) > C_b > 3.8×10^{-3} (at section 6). The predicted interface elevations at sections 2 and 6 (Fig. 1) are then used in the evaluation of Eq. (6) for corresponding internal heads, from which the internal head losses $\Delta E^*_{I\,(2)\rightarrow(6)} \approx 0.53 \times 10^{-3}$ (for $\phi = 3.6°$) and 1.02×10^{-3} (for $\phi = 1.7°$) are estimated. These results indicate that frictional dissipation due to bed friction alone will be approximately twice as large for $\phi = 1.7°$ than for $\phi = 3.6°$. However, within the experiments, the overall effect of bottom friction alone is considered to be marginal, as evidenced by calculated discharge coefficients C_d [Eq. (5)] being only slightly lower than unity ($C_d > 0.99$) for all runs.

Differences in the interfacial mixing characteristics between the steeper and milder slope runs have been previously highlighted by the observed longitudinal variations in pycnocline structure (see §3 and Fig. 7). For the $\phi = 3.6°$ runs, the interfacial drag coefficient C_i required to fit reduced gravity hydraulic model predictions to experimental measurements was found to be approximately constant [$C_i \approx 0.0255$, see Fig. 9a], with corresponding discharge coefficient $C_d \approx 0.91$ [calculated for interfacial friction only, Eq. (5)] for all Q_1 values. These constant (C_i, C_d) values confirm that the internal structure of the dense bottom current is self-similar for all $\phi = 3.6°$ runs. Such frictionally-controlled internal flow cases are represented by an accelerating flow in the along-channel direction, with isopycnals converging towards sill section 6 [see Fig. 7a]. Combining the effects of bottom and interfacial friction (by specifying $C_f = C_b + C_i$ in the reduced gravity model), the total internal head loss $\Delta E^*_{I\,(2)\rightarrow(6)} \approx 5.7 \times 10^{-3}$, which is shown to be an order of magnitude larger than the predicted head loss from bottom friction alone.

For the $\phi = 1.7°$ runs, the reduced gravity model failed to predict the measured longitudinal variations in interface elevation under the implicit assumptions of conserved

lower layer volumetric flux ($dQ_1/dy = 0$) and stratification ($dg'/dy = 0$) along the converging channel [Fig. 9b]. These hydraulically-controlled dense bottom outflows are shown [Fig. 7b] to exhibit pycnocline divergence towards the sill section 6 [see Fig. 7b], indicating ambient water entrainment into the lower layer, which changes the volume flux and dilutes the bottom gravity current. However, the internal head can be estimated [Eq. (6)] at sections 2 and 6 directly from measured interface $\rho' = 0.5$ elevations [i.e. at P3 and P6, respectively, Fig. 2b] and the corresponding lower layer volume flux, estimated from the ADV velocity profiles [Fig. 2b]. The corresponding total head loss was thus estimated to be $\Delta E^*_{I\,(2)\to(6)} \approx 0.0244$, which is approximately 25 times larger than for bed friction alone. Thus the total internal head loss estimates for the milder bed slope are much larger than in the steeper bed.

6 Discussion

6.1. *Interfacial Stability Analysis*

Distinct differences have been noted (§3 and §5) in the longitudinal internal structure of the pycnocline for the two bed slope cases. This structure was, however, found to be largely self-similar in the transverse (x) direction, with uniform pycnocline thickness Δh observed across the vee-shaped channel. This was also apparent from measured ADV velocity profiles, where the maximum core velocities v_{max} of the outflowing lower layer were also shown to remain largely unchanged across the channel width within individual runs. A turbulence parameter useful for characterising the internal structure of the outflowing bottom layer is the interfacial Reynolds stress $\rho\overline{v'w'}$ (where v' and w' are the instantaneous longitudinal and vertical velocity fluctuations at the interface elevation). Dependence of this Reynolds stress on velocity shear dv/dz and density stratification $d\rho/dz$ is usually characterised by the gradient Richardson number $\mathrm{Ri}_g = N^2(z)/(dv/dz)^2$, where $N(z)$ is the Brunt-Väisälä frequency [with $N^2(z) \equiv -(g/\rho)(d\rho/dz)$]. A necessary condition for linear stability in inviscid, stratified, parallel and horizontal shear flows is defined when $\mathrm{Ri}_g > 1/4$. Under such conditions, turbulence production $P = -\overline{v'w'}\,(dv/dy)$ due to Reynolds stress and shear is comparatively small [i.e. interfacial mixing processes are suppressed by stratification (e.g. Holt *et al*. 1992)]. By contrast, while $\mathrm{Ri}_g < 1/4$ defines a necessary condition for interfacial instability, it does not guarantee that such instabilities will occur.

The gradient Richardson number Ri_g close to the pycnocline can be approximated by a finite-difference relationship $\mathrm{Ri}_g = g(\Delta\rho/\rho)\Delta h/(\Delta v)^2$ (Osborn 1980). In this relationship, Δv and $\Delta\rho$ are the vertical change in velocity and density, respectively, across pycnocline thickness Δh, defined by difference in elevation between isopycnals $\rho' = 0.4$ and $\rho' = 0.6$. In the $\phi = 3.6°$ runs, the density gradient $d\rho/dz$ is shown to be comparatively stronger than the

velocity gradient dv/dz across the pycnocline [see Fig. 6a]. The estimated values of $\mathrm{Ri}_g > 1.51$ thus correspond well to the stable stratification and strongly-inhibited turbulent mixing observed in these runs. For the $\phi = 1.7°$ runs, the relative weakness of the density gradient dρ/dy compared to the velocity gradient dv/dy across the pycnocline [see Fig. 6b] demonstrates that the estimated values of $\mathrm{Ri}_g < 0.6$ correspond potentially to somewhat weakened stratification and stronger shear-generated turbulent mixing (but not necessarily small enough to create instabilities). [It is noted that, with this assumed linearization across the pycnocline, only the $\phi = 1.7°$ run with $Q_1 = 0.9$ l s^{-1} provides an estimated Ri_g value (= 0.16) that is lower than the defined linear stability criterion $\mathrm{Ri}_g > 1/4$]. Gradient Richardson number $\mathrm{Ri}_g(y)$ profiles were also estimated directly for both $\phi = 3.6°$ and 1.7° runs [Fig 10a and 10b, respectively] through the measured density and velocity profiles obtained adjacent to sill section 6 (see Fig. 2). Here, the maximum values of $\mathrm{Ri}_g > 2.1$ and minimum values of $\mathrm{Ri}_g < 0.37$, obtained in the vicinity of the $\rho' = 0.5$ isopycnal elevation for the $\phi = 3.6°$ and 1.7° cases, respectively, are in general agreement with the linearized values obtained previously. In this case, for the $\phi = 1.7°$ runs with $Q_1 = 0.6$ and 0.9 l s^{-1}, the estimated Ri_g values [= 0.26 and 0.08, respectively, see Fig. 10(b)] are close to or lower than the linear stability criterion $\mathrm{Ri}_g > 1/4$.

6.2. *Interfacial Mixing and Entrainment*

Dilution of the dense water layer by the overlying fresh ambient water may result in both an along-channel reduction in stratification (i.e. through g') and a corresponding increase in outflowing lower layer volume flux Q_1. Thus, the changes of these two potential effects can be confirmed by estimating local values of the lower layer mass flux $\Pi_1 = \rho_1 Q_1$, as well as its change from initial source conditions. Following this approach, local values of the stratification g' and volume and mass fluxes, Q_1 and Π_1, respectively, can be estimated at sill section 6 from the integration of measured velocity $v(z)$ and density $\rho(z)$ profiles (e.g. Girton *et al.* 2006) between the bed z_b and interface ($z_b + h_1$) elevations, such that:

$$\overline{v}_1 = \frac{2}{h_1^2} \int_{z_b}^{z_b + h_1} v(z)\, z \, \mathrm{d}z \,, \tag{7}$$

$$g' = \frac{g}{\rho_1 h_1} \int_{z_b}^{z_b + h_1} \left(\rho(z) - \rho_0 \right) \mathrm{d}z \,, \tag{8}$$

where $\overline{v}_1$ is the average lower layer outflow velocity at sill section 6. Hence, the lower layer volume Q_1 and mass Π_1 fluxes can be defined, using Eq. (7), for the vee-shaped channel with side slope α [= tan(33°)] at sill section 6, *viz.*

$$Q_1 = \bar{v}_1 \frac{h_1^2}{\alpha} = \frac{2}{\alpha} \int_{z_b}^{z_b+h_1} v(z)\, z\, dz \qquad (9)$$

$$\Pi_1 = \frac{2}{\alpha} \int_{z_b}^{z_b+h_1} \rho(z)\, v(z)\, z\, dz \qquad (10)$$

Direct comparisons between the upstream source conditions (Q_1, g' and Π_1) and the corresponding values obtained at sill section 6 from Eqs. (8) - (10) are given in Table 1 for all ϕ = 3.6° and 1.7° runs. In calculating g' from Eq. (8), it is noted that ρ_1 and ρ_0 are the locally-defined maximum and minimum values obtained from the mean density profiles at sill section 6. In addition, these local g' values (shown in Table 1) are calculated by integrating the mean density profiles up to the ρ' = 0.5 elevation (i.e. setting h_1 to the nominally-defined interface), in order to provide an indication of the magnitude of net entrainment effects on stratification along the up-sloping, converging channel.

For the solution of flux Eqs. (9) and (10), h_1 is defined by the elevation at which $v(z)$ = 0, in order to capture the full Q_1 and Π_1 fluxes associated with the outflowing water layer, i.e. $Q_1(z)$ and $\Pi_1(z) \rightarrow const.$, as $v(z) \rightarrow 0$. Within the ϕ = 3.6° runs, Q_1 remains relatively unchanged between the channel inlet (Fig. 1) and sill section 6, with an average increase in volume flux ΔQ_1 = 0.76% and well conserved mass flux i.e. $\Delta\Pi_1 < 0.6\%$ (see Table 1). This is again indicative of stable stratification and limited interfacial mixing for ϕ = 3.6°, which results in only a marginal net entrainment of overlying fresh ambient fluid into the dense outflowing bottom layer [as indicated by the relatively small reduction in g' values along the channel (up to 7%), see Table 1]. For the ϕ = 1.7° runs, the average increase in volume flux is significantly higher at ΔQ_1 = 9.69%, with a small error in the mass flux conservation, i.e. $\Delta\Pi_1 < 1.9\%$, predicted between the channel inlet and sill section 6 (Table 1). This is clearly indicative of strong net entrainment effects of ambient fluid into the dense outflowing bottom layer, leading to the observed increase in volume flux Q_1 and a significant reduction (through lower layer dilution) in g' = 0.127 → 0.084 m s^{-2} (i.e. ~35%, Table 1) between the channel inlet and sill section 6.

6.3. *Definition of Interface Elevation*

The experiments have shown that it is not entirely straightforward to define the interface elevation h_1 in all experimental runs. This is particularly pertinent for ϕ =1.7°, where strong interfacial mixing/net entrainment effects result in variation in the relative elevations of (i) the ρ' = 0.5 isopycnal (nominally selected to represent the interface), (ii) the normalised interfacial velocity v/v_{max} = 0.5, and (iii) the maximum density and velocity gradients, $(d\rho/dz)_{max}$ and $(dv/dz)_{max}$, respectively. Under the assumption of inviscid two layer flow, the

integral quantities $\bar{v}_1$ and g' [Eqs. (7), (8)] will remain constant up to the defined interface h_1 between the two layers (i.e. $\bar{v}_1 = v_1$ and $g' = g(\rho_1 - \rho_0)/\rho_1$, by definition). However, for the depth-varying density and velocity profiles obtained in the experiments, calculated $\bar{v}_1$ and g' values are clearly dependent on the specification of h_1 in the integrals [Eq. (7), (8)] and are thus defined nominally as functions in z [$\bar{v}_1(z)$ and $g'(z)$, respectively].

This uncertainty over the interface definition also has crucial implications for the determination of the composite Froude number G^2 in the two-layer flow approximation at sill section 6. According to Laanearu and Davies (2007), G^2 can be defined for a triangular channel cross-section by the formula:

$$G^2 = 2\frac{\bar{v}_0^2}{g'}\frac{h_1}{\left(H^2 - h_1^2\right)} + 2\frac{\bar{v}_1^2}{g'h_1}, \qquad (11)$$

where $\bar{v}_0$ is the average velocity in the upper layer. With $\bar{v}_1$ and g' values dependent on h_1, as before, a profile of composite Froude number $G^2(z)$ can nominally be obtained through substitution of $\bar{v}_1(z)$ and $g'(z)$ into Eq. (11) for a range of h_1 values (e.g. $h_1 = 0 \rightarrow H$).

Figs. 11a and 11b present these $G^2(z)$ profiles plotted against normalised depth $(z - z_b)/H$ (= h_1/H) for the $\phi = 3.6°$ and 1.7° bed slopes, respectively. Data points (+) shown on these profiles indicate the calculated G^2 values at the $\rho' = 0.5$ isopycnal elevation (i.e. the nominally-defined density interface). In the $\phi = 3.6°$ runs [Fig. 11a], the G^2 values at this elevation range from $G^2 \approx 0.31 \rightarrow 0.42$ (for $Q_1 = 0.3 \rightarrow 0.9$ l s^{-1}) and, as such, are in broad agreement with the predicted single layer densimetric Froude number range $F_1^2 = 0.44 \rightarrow 0.47$.

It is apparent from Fig. 11b that, for $\phi = 1.7°$ runs, G^2 values of about $1.0 \rightarrow 1.4$ occur at the $\rho' = 0.5$ elevation (for $Q_1 = 0.3 \rightarrow 0.9$ l s^{-1} runs). This indicates that critical (or mildly supercritical conditions, i.e. $G = 1.0 \rightarrow 1.18$) are obtained at sill section 6 when h_1 is specified as the $\rho = 0.5$ elevation. On closer inspection of these $G^2(z)$ profiles [Fig. 11b], critical internal flow conditions (i.e. $G^2 = 1.0$) are shown to occur at different $\rho' \leq 0.5$ isopycnal elevations within the outflowing layer (i.e. $\rho' \approx 0.49$, 0.27 and 0.18 for $Q_1 = 0.3$, 0.6 and 0.9 l s^{-1}, respectively). This indicates that, in the two-layer flow assumption, the selection of the $\rho' = 0.5$ isopycnal may not always be most appropriate to represent the interface elevation between the outflowing dense water and ambient fluid for hydraulically-controlled internal flow conditions. It is interesting to note that the representative isopycnal elevations corresponding to the peak density gradients in the $\phi = 1.7°$ runs [see, for example, Fig. 6b] are $\rho' \approx 0.38$, 0.31 and 0.28 for $Q_1 = 0.3$, 0.6 and 0.9 l s^{-1}, respectively. In this sense, they are in

good accord with the physically-relevant interfacial elevations determined in the two-layer flow approximation ($G^2 = 1.0$) above [see Fig. 11b].

6.4. *Interfacial Stresses*

An estimation of the actual interfacial stress τ_i can be obtained through the established formula $\tau_i/\rho = C_i\, v_i^2$ (c.f. Sargent and Jirka 1987), where the interfacial velocity $v_i = v_{1,max}/2$ (with $v_{1,max}$ defined as the maximum lower layer outflow velocity). Thus, for the $\phi = 3.6°$ velocity profile data [see Fig. 5a], $v_{1,max} = 0.029$, 0.041 and 0.047 m s^{-1} for $Q_1 = 0.3$, 0.6 and 0.9 l s^{-1}, respectively; and specifying $C_i = 0.0255$ (as before), the estimated interfacial stresses are represented by $\tau_i/\rho = 0.054$, 0.112 and 0.149 cm^2 s^{-2} (see Table 2). This total interfacial stress is transferred into sheared motion of the upper salted and lower diluted water layers through a combination of (i) viscous stress $\nu.\mathrm{d}v_i/\mathrm{d}z$ (where ν is the kinematic viscosity of water); (ii) turbulent (Reynolds) stress $\overline{v_i' w_i'}$ (where v_i', w_i' are interfacial velocity fluctuations); and (iii) net entrainment effects $w_{ei}.v_i$ (where w_{ei} is the net entrainment velocity). An estimate of w_{ei} is obtained from the change in volume flux ΔQ_1 between the channel inlet and sill section 6, through the following approximate expression: $w_{ei} = \Delta Q_1 \tan(\alpha)/(2Lh_1)$, where L is the converging channel length.

Considering the $\phi = 3.6°$ runs, the viscous stress component, obtained directly from measured peak velocity gradients $\mathrm{d}v_i/\mathrm{d}y$ at the interface [see Figs. 5a and 6a], is shown to contribute approximately 20% - 30% of the total interfacial stress (Table 2). By contrast, the net entrainment effects are expected to be negligible as the internal flow has been demonstrated to remain stably-stratified along the channel for $\phi = 3.6°$, with only marginal mixing and entrainment at the interface. Indeed, with the estimated net entrainment velocities w_{ei} ranging from 3.28 $\rightarrow$ 7.29 ($\times 10^{-6}$) m s^{-1}, the resulting net entrainment effect $w_{ei}.v_i$ are shown to contribute only 0.9% $\rightarrow$ 1.2% of the total interfacial stress (Table 2). The remaining contribution is therefore due to the Reynolds stress $\overline{v_i' w_i'}$, which, for the $\phi = 3.6°$ runs, is estimated to contribute between approximately 62% - 78% to the total interfacial stress.

The measured increase in the dense outflowing layer volume flux Q_1, and corresponding reduction of g', indicate strong net entrainment and dilution in the lower outflowing layer for the $\phi = 1.7°$ runs. As a consequence, the reduced gravity hydraulic model (§4) failed to predict the measured along-channel interface ($\rho' = 0.5$) elevations for these runs [Fig. 9b], meaning that a universal interfacial friction coefficient C_i could not be specified under the assumption of conserved stratification g' and volume flux Q_1 along the channel. However, by considering a shorter section of the converging channel (section 5 $\rightarrow$ 6, Fig. 1), model predictions were more-or-less well fitted to experimental measurements [at P5 and P6,

Fig. 2b] by specifying $C_i \approx 0.0088$, and larger Q_1 and reduced g' values obtained through integration of velocity and density profiles at sill section 6 [i.e. Eqs. (8) and (9), respectively]. With these assumptions, the total interfacial stress can be estimated for the $\phi = 1.7°$ runs to range from $\tau_i/\rho = 0.075 \rightarrow 0.140$ cm^2 s^{-2} (Table 2). The contribution from the viscous stress component $\nu dv_i/dy$ is shown to increase (compared to the $\phi = 3.6°$ runs) to between 34% - 43% (Table 2), due to larger velocity gradients in the $\phi = 1.7°$ runs [see Fig. 5b]. As expected, net entrainment effects $v_i.w_{ei}$ are shown to have a significantly larger contribution in the $\phi = 1.7°$ runs, increasing to about 22% - 30% of the total interfacial stress (compared to just 0.5 - 0.6% for $\phi = 3.6°$, see Table 2). It can therefore be concluded that this combined increase in viscous stress contributions (13.2% on average) and net entrainment effects (24.4% on average) in the $\phi = 1.7°$ runs leads to an average reduction of 37.6% in the Reynolds stress contribution to the total interfacial stress, when compared with the $\phi = 3.6°$ runs (Table 2).

7. Conclusions

The analysis of detailed laboratory measurements presented herein allowed the dynamics of dense bottom gravity currents propagating along in a vee-shaped and converging channel to be compared for two different adverse bed slope conditions. Whilst providing an experimental dataset for future validation of improved numerical models of stratified flows, the main purpose of the study was to explore the application of simple hydraulic modelling approaches to describe the pertinent features of such topographically-constrained dense bottom gravity currents.

For the quasi-equilibrium outflows generated within the basin and converging channel sections under different steady state volumetric inflow conditions, frictional effects due to smooth channel bottom boundary were minimal, with the main source of internal dissipation arising from interfacial processes between the outflowing bottom gravity current and overlying ambient water.

The two topographic situations tested (with adverse bed slope angles $\phi = 3.6°$ and 1.7°) exhibited different interfacial dynamics. For the steeper, up-sloping channel ($\phi = 3.6°$), the internal flow structure was characterised by a sharp pycnocline and decreasing isopycnal separation between the upper quiescent water and dense bottom current in the along-channel direction. Correspondingly, the volume flux Q_1 remained relatively unchanged between the deep-water motions in the inlet basin and the dense water outflow at the sill section. For this topographic case, the reduced gravity hydraulic model was found to predict successfully the along channel interface elevation for all volumetric inflows. These dense water outflows were found to correspond to frictionally-controlled situations (i.e. $F_1 < 1$). By contrast, for the milder, up-sloping channel ($\phi = 1.7°$), more complex internal flow dynamics were observed,

associated with increasing isopycnal separation in the along-channel direction and an average increase in volume flux ΔQ_1 = 9.69% between the inlet and sill sections. This was due to strong net entrainment of the ambient water into the dense outflowing bottom layer, leading to a significant reduction in the reduced gravity along the channel. For this topographic case, the dense water outflow was also found to be hydraulically-controlled (i.e. $G \rightarrow 1$) near the sill section. The importance of interfacial mixing in such cases has been recognised by Hebbert *et al.* (1979), who have shown the necessity of including an interfacial stress term in the reduced gravity hydraulic model (as here in Eq. (3), where C_f includes a contribution from the interfacial stress). Note that one implication of the approach in Hebbert *et al.* (1979) is that bottom friction dominates the mixing at the interface for the type of mild slopes and rough boundaries found in the field.

While stable stratification and strongly-inhibited turbulent mixing was observed in the $\phi = 3.6°$ runs, the relatively weakened density gradient ($d\rho/dy$) in the $\phi = 1.7°$ runs, compared to the velocity gradient (dv/dy), corresponds to a potentially unstable situation and stronger shear-generated turbulent mixing across the pycnocline. This was manifested in the gradient Richardson number (Ri_g) predictions at the sill-section interfacial zone, which were close to or lower than the critical value Ri_g = 1/4 for linear stability under the milder bed slope condition. Such unstable situations, due to creation of stratified flow instabilities, are typically found in the tidal estuaries (e.g. Carpenter *et al.* 2007, Tedford *et al.* 2009). Further investigations of stratified-flow dynamics in the non-rectangular channels are thus needed to parameterize, for example, buoyancy fluxes and quantify these mixing effects.

Acknowledgements

Financial support was provided through a Distinguished Visiting Fellowship award to J.L. from The Royal Academy of Engineering (UK) tenable at the University of Dundee. Further support was awarded to A.J.S.C. from The Royal Society of Edinburgh (RSE) International Exchange programme. The experimental work was funded through the EU FP6 HYDRALAB III Programme (Contract no. 022441), which facilitated a series of laboratory measurements at the Coriolis Laboratory in NTNU, Trondheim, Norway. The technical support of Prof. Thomas McClimans and his team in Trondheim is gratefully acknowledged. The authors also acknowledge the insightful comments of anonymous reviewers that led to significant improvements in the paper.

Notation

C_f = combined quadratic law friction coefficient [$C_f = C_b + C_i$] (-)

C_d = discharge coefficient (-)

E = specific energy (m)

f = Darcy-Weisbach friction factor (-)

F = densimetric Froude number (-)

G = composite Froude number (-)

g = acceleration due to gravity (m s^{-2})

g' = reduced gravity (m s^{-2})

H = in-channel water depth (m)

h = water layer thickness (m)

i = bed slope (-)

K_i = internal-energy parameter [internal head] (m)

K_{ii} = lower-layer volume flux parameter (-)

L = channel length (m)

R = hydraulic radius [$R = R_b + R_i$] (m)

Ri_g = gradient Richardson number (-)

R_c = channel Reynolds number (-)

u = cross-channel velocity component (m s^{-1})

v = along-channel velocity component (m s^{-1})

v' = instantaneous longitudinal velocity fluctuation (m s^{-1})

w = vertical velocity component (m s^{-1})

w' = instantaneous vertical velocity fluctuation (m s^{-1})

w_{ei} = net entrainment velocity (m s^{-1})

q = ratio of upper and lower layer volume fluxes (-)

x = cross-channel coordinate (m)

y = along-channel coordinate (m)

z = vertical coordinate (m)

Q = volume flux (m^3 s^{-1})

α = channel side-slope (-)

ΔE_I = internal-head loss (m)

ϕ = adverse bed slope angle (°)

ν = kinematic viscosity (m^2 s^{-1})

Π = mass flux (m^4 s^{-3})

θ = side slope angle (°)

ρ = water density (kg m^{-3})

ρ_0 = ambient water density (kg m^{-3})

ρ_1 = bottom water density (kg m^{-3})

ρ' = density excess [$\rho' = (\rho - \rho_0)/(\rho_1 - \rho_0)$] (-)

χ = wetted perimeter (m)

References

Arita, M., Jirka, G.H. (1987a). Two-layer model of saline wedge. I: Entrainment and interfacial friction. *J. Hydraul. Engng.,* ASCE 113(10), 1229–1248.

Arita, M., Jirka, G.H. (1987b). Two-layer model of saline wedge. II: Predictions of mean properties. *J. Hydraul. Engng.,* ASCE 113(10), 1249–1263.

Armi, L. (1986). The hydraulics of two flowing layers of different densities. *J. Fluid Mech.*, 163, 27–58.

Armi, L., Farmer, D.M. (1986). Maximal two-layer exchange through a contraction with barotropic net flow. *J. Fluid Mech*., 164, 27–51.

Baines, P.G. (1984). A unified description of two-layer flow over topography. *J. Fluid Mech*., 146, 127–167.

Borenäs, K., Lundberg, P. (1988). On the deep-water flow through the Faroe Bank Channel. *J. Geophys. Res*., AGU 93(C2), 1281–1292.

Cuthbertson, A.J.S., Davies, P.A., Coates, M.J., Guo, Y. (2004). A modelling study of transient, buoyancy-driven exchange flow over a descending barrier. *Environ. Fluid Mech.*, 4, 127–155.

Cuthbertson, A.J.S., Laanearu, J., Davies, P.A. (2006). Buoyancy-driven two-layer exchange flows across a slowly submerging barrier. *Environ. Fluid Mech.*, 6, 133–151.

Cuthbertson, A.J.S., Laanearu, J., Wåhlin, A.K., Davies, P.A. (2011). Experimental and analytical investigation of dense gravity currents in a rotating, up-sloping and converging channel. *Dynamics of Atmospheres and Oceans*, 52(3), 386–409.

Dalziel, S.B. (1991). Two-layer hydraulics: a functional approach. *J. Fluid Mech.*, 223, 135–163.

Dalziel, S.B. (1992). Maximal exchange in channels with nonrectangular cross sections. *J. Phys. Oceanogr*., AMS 22, 1188–1206.

Davies, P.A. (2006). *Mixing and Dispersion in Stably Stratified Flows*. The Institute of Mathematics & Its Application Conference Series Number 68. Oxford University Press, Oxford, U.K.

Davies, P.A., Wåhlin, A.K., Guo, Y. (2006). A combined laboratory and analytical study of flow through the Faroe Bank Channel. *J. Phys. Oceanogr.*, AMS 36, 7, 1348–1364.

Farmer, D.M., Armi, L. (1986). Maximal two-layer exchange over a sill and through the combination of a sill and contraction with barotropic flow. *J. Fluid Mech*., 163, 27–58.

Fristedt, T., Lundberg, P., Sigray, P. (2005). Technical note on possible hydraulic control of the exchange through the Oxdjupet passage in the Baltic Sea. *Estuarine, Coastal and Shelf Science*, 65(3), 526–534.

Girton, J.B., Pratt, L.J., Sutherland, D.A., Price, J.F. (2006). Is the Faroe Bank Channel overflow hydraulically controlled?. *J. Phys. Oceanogr.*, AMS 36, 2340–2346.

Hebbert, R., Imberger, J., Loh, I., Patterson, J.C. (1979). Collie River underflow into the Wellington Reservoir, *Journal of the Hydraulics Division*, ASCE 105(HY5), 533–545.

Hogg, A., Ivey, G., Winters, K. (2001). Hydraulics and mixing in controlled exchange flows. *J. Geophys. Res.*, AGU 106(B), 959–972.

Ivey, G.N. (2004). Stratification and mixing in sea straits. *Deep-Sea Res. II*, 51, 441–453.

Ivey, G.N., Imberger, J. (1991). On the nature of turbulence in a stratified fluid. Part I: the energetics of mixing. *J. Phys. Oceanogr.*, AMS 21, 650–658.

Jackson, C.M. García, K.A. Oberg, K.K. Johnson, M. H. García (2008). Density currents in the Chicago River: Characterization, effects on water quality, and potential sources. *Science of The Total Environment*, 401, 130–143.

Kõuts, T., Omstedt, A. (1993). Deep-water exchange in the Baltic Proper. *Tellus*, 45(A), 311–324.

Laanearu, J., Vassiljev, A., Davies, P.A. (2011). Hydraulic modelling of stratified bi-directional flow in a river mouth. *IOC Engineering and Computational Mechanics***,** 164(EM1), 207–216.

Laanearu, J. and Davies, P.A. (2007). Hydraulic control of two-layer flow in 'quadratic'-type channels. *J. Hydr. Res*., IAHR 45(1), 3–12.

Laanearu, J., Lundberg, P. (2005). Analysis and improvement of a perturbation solution for hydraulic flow in a rotating parabolic channel. *ZAMM · Z. Angew. Math. Mech*., 85(7), 490-498.

Laanearu, J., Lundberg, P. (2003). Topographically constrained deep-water flows in the Baltic Sea. *J. Sea Res*., 49(4), 257-265.

Laanearu, J., Koppel, T., Soomere, T., Davies, P.A. (2007). Joint Influence of River Stream, Water Level and Wind Waves on the Height of Sand Bar in a River Mouth. *Nordic Hydrology*, 38(3), 287-302.

Lorke, A., Peeters, F., Wüest, A. (2005). Shear-induced convective mixing in bottom boundary layers on slopes. *Limnol. Oceanogr.*, 50(5), 1612-1619.

Osborn, T.R. (1980). Estimates of the local rate of vertical diffusion from dissipation measurements. *J. Phys. Oceanogr.*, AMS 10, 83-89.

Pratt, L.J., Whitehead, J.A. (2007). *Rotating Hydraulics: Nonlinear Topographic Effects in the Ocean and Atmosphere*. Springer Science + Business Media, LLC, New York, U.S.A.

Pratt, L.J. (1986). Hydraulic control of sill flow with bottom friction. *J. Phys. Oceanogr*, AMS 16, 1970-1980.

Sargent, F.H., Jirka, G.H. (1987). Experiments on the saline wedge. *J. Hydraul. Engng.*, ASCE 113(10), 1307-1324.

Schijf, J.B., Schonfeld, J.C. (1953). Theoretical considerations on the motion of salt and fresh water. *Proc., Minnesota Int. Hydr. Conv., ASCE and IAHR, Minneapolis, Minn*. 321-333.

Stenström, P. (2003). Mixing and recirculation in two-layer exchange flows. *J. Geophys. Res.*, AGU 108(C8), 1201-1213

Zhu, D.Z., Lawrence, G.A. (2000). Hydraulics of exchange flows. *J. Hydraul. Engng.*, ASCE 126(12), 921–928.

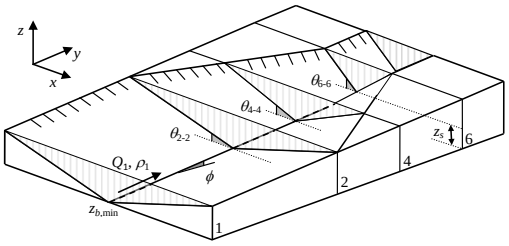

Section	α (°)	W (m)	Y (m)
1	14.8	2.50	-3.000
2	14.8	2.50	-1.500
3	16.6	2.08	-1.125
4	19.4	1.65	-0.750
5	23.8	1.23	-0.375
6	33.0	0.80	0.000
7	33.0	0.80	0.500

(a)

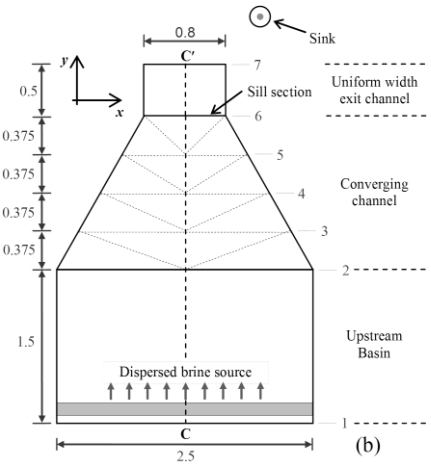

(b)

Figure 1 (a) 3D schematic representation of channel topography, and (b) plan view (*xy* plane) of the channel showing main dimensions. Cross-sectional side slopes (α) and maximum channel widths (W) at cross sections 1 - 7 are tabulated.

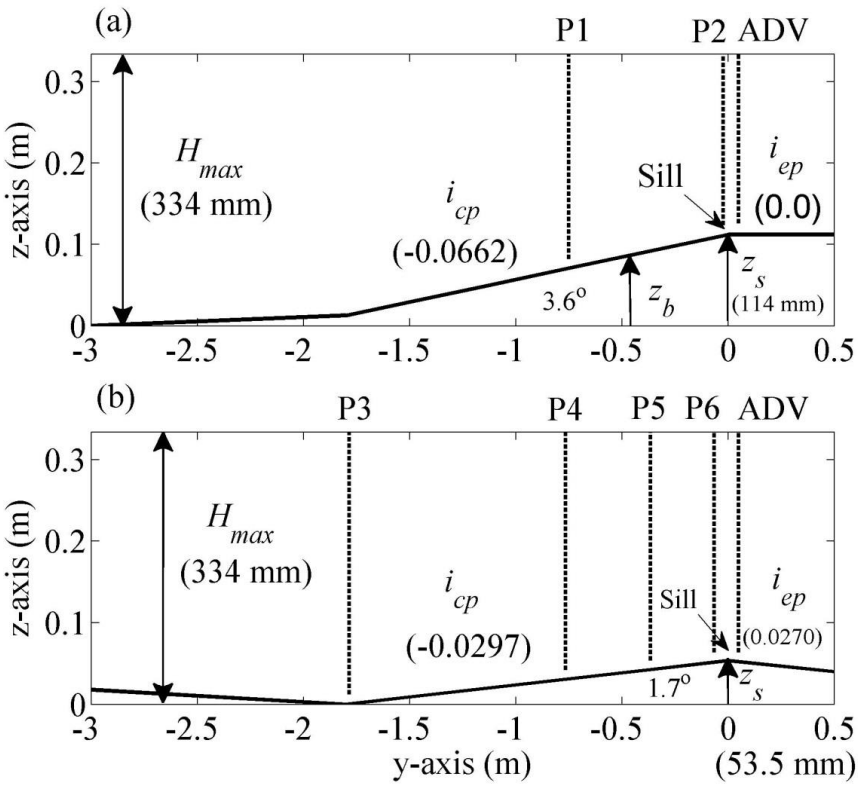

Figure 2 Centreline channel bed topography (*yz* plane) for adverse, along-channel bed slopes of (a) $\phi = 3.6°$ and (b) $\phi = 1.7°$ in the converging channel section.

Comment [AC1]: Think we should make font size of axis labels, numbers, and variables smaller. This probably goes for all Figures.

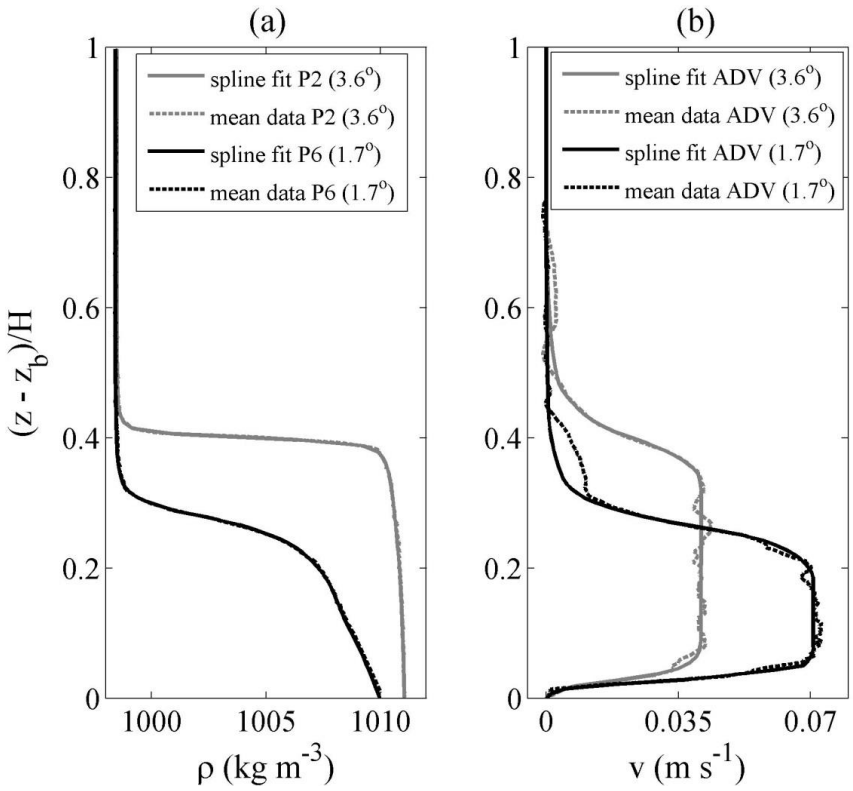

Figure 3 Measured data (dashed profiles) and fitted splines (solid profiles) for (a) density and (b) velocity. Density probes P7 (ϕ = 3.6°) and P6 (ϕ = 1.7°) and ADV data are presented for volumetric inflow Q_1 = 0.6 l s^{-1}.

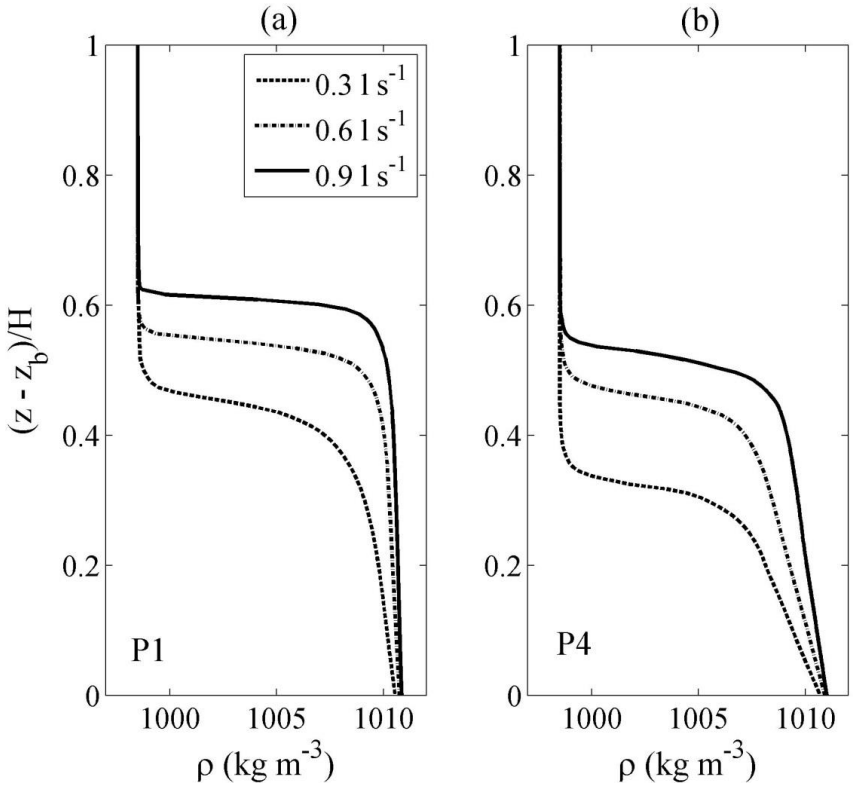

Figure 4 Fitted splines profiles of mean density data for density probe locations (a) P1 (ϕ = 3.6°), and (b) P4 (ϕ = 1.7°) under volumetric inflows Q_1 = 0.3, 0.6, 0.9 l s^{-1}.

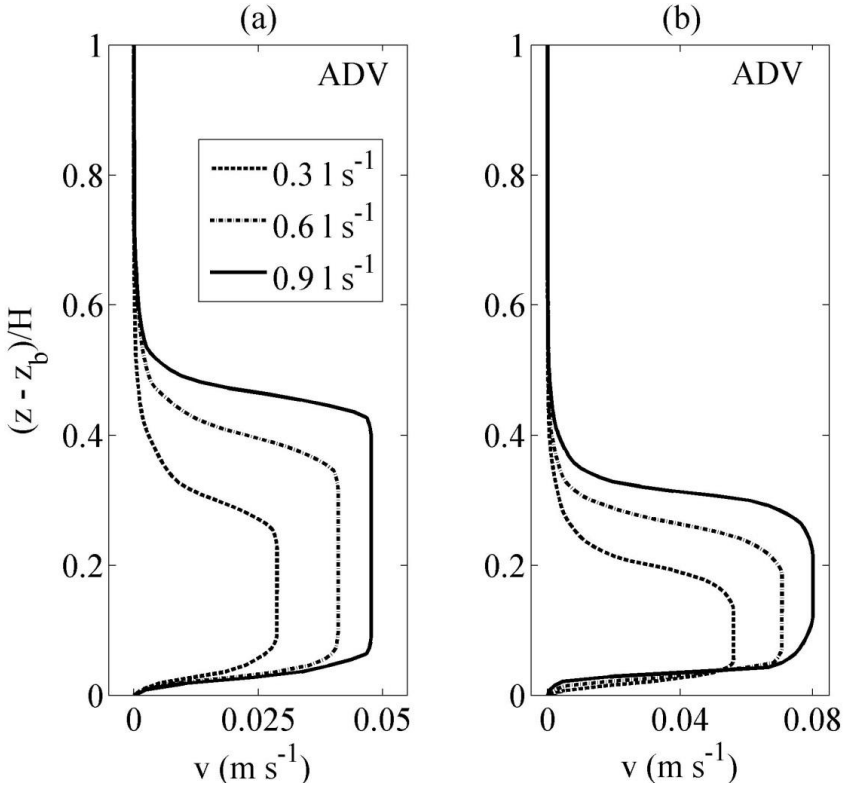

Figure 5 Fitted splines profiles of mean velocity data from ADV location for bed slope conditions of (a) $\phi = 3.6°$, and (b) $\phi = 1.7°$, under volumetric inflows $Q_1 = 0.3, 0.6, 0.9$ l s^{-1}.

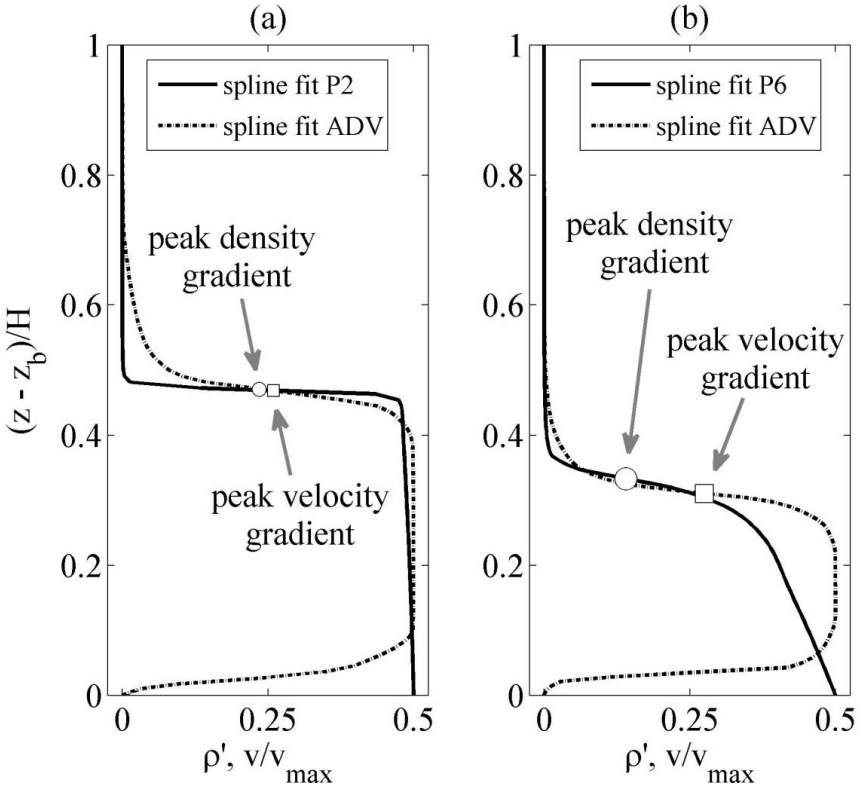

Figure 6 Combined plots of density excess ρ' and normalised velocity v/v_{max} profiles for bed slope conditions of (a) ϕ = 3.6° (density probe P7), and (b) ϕ = 1.7° (density probe P6), and volumetric inflow Q_1 = 0.9 l s^{-1}.

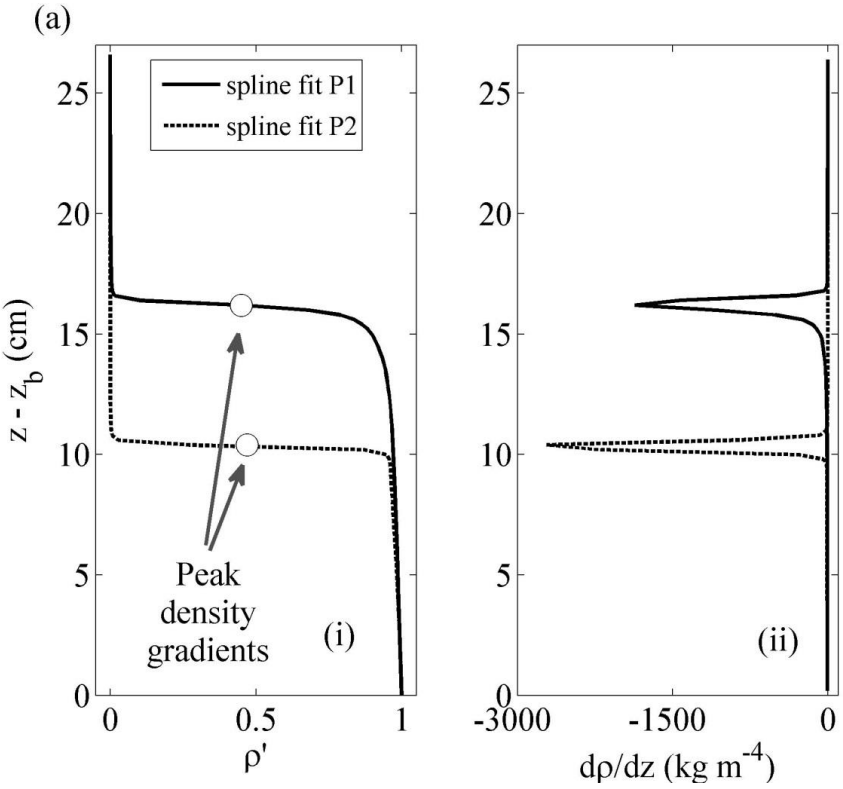
(a)
spline fit P1
spline fit P2
Peak
density
gradients
(i)
(ii)
z - z_b (cm)
ρ'
dρ/dz (kg m^-4)
0
5
10
15
20
25
0
0.5
1
-3000
-1500
0

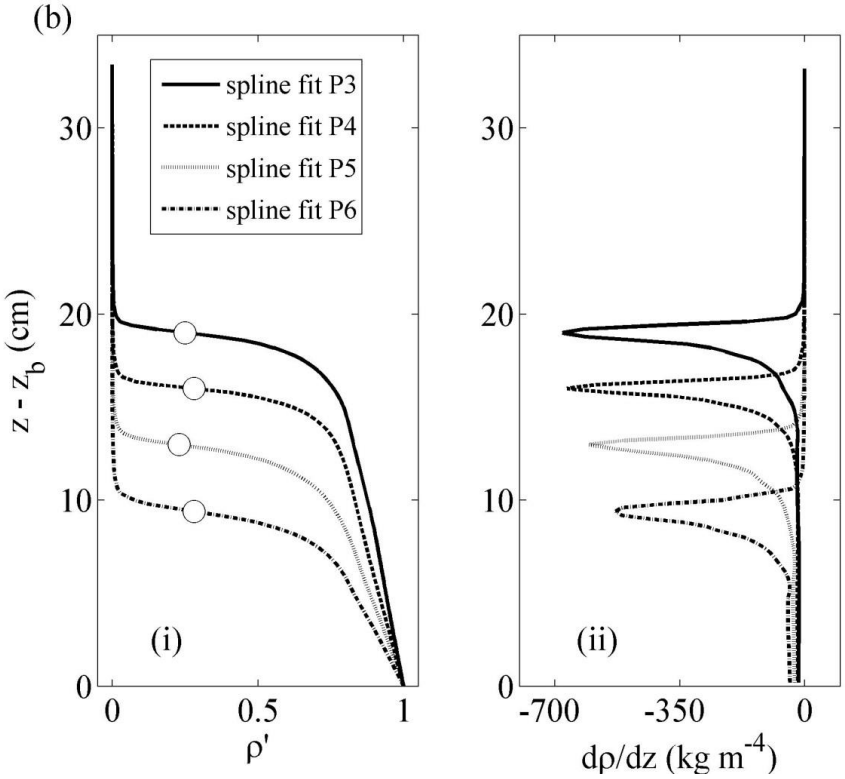

Figure 7 Combined plots of (i) density excess ρ' and (ii) density gradient ($d\rho/dz$) profiles along converging channel for bed slope conditions of (a) $\phi = 3.6°$, and (b) $\phi = 1.7°$, and volumetric inflow $Q_1 = 0.9\ l\ s^{-1}$.

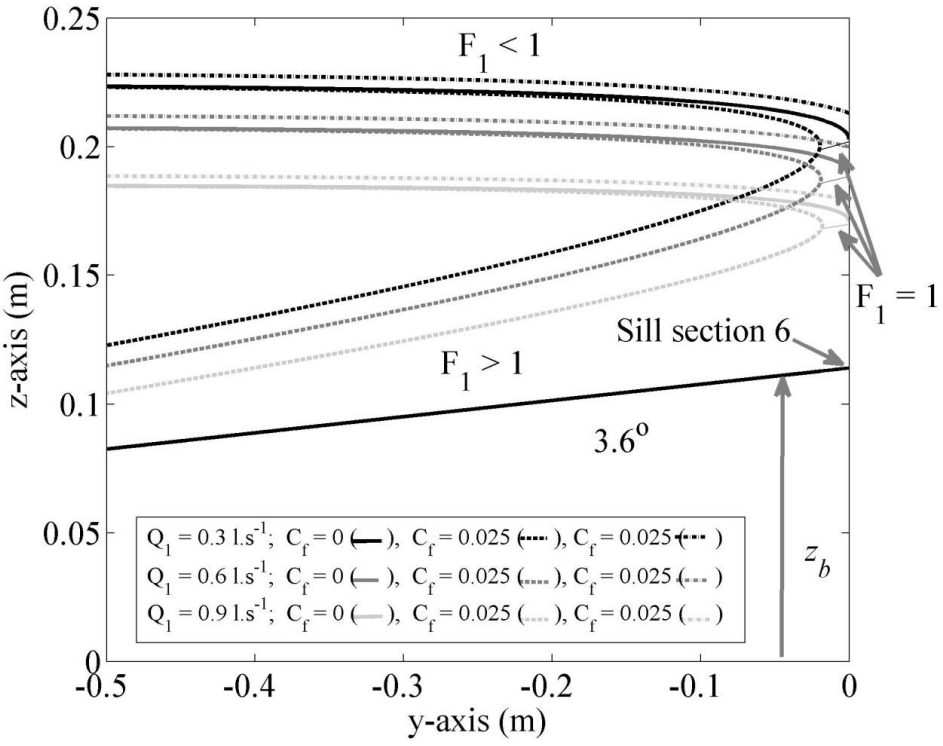

Figure 8 Reduced gravity hydraulic model predictions of interface elevation along converging, vee-shaped channel for bed slope $\phi = 3.6°$. Inviscid (solid curves) and frictional ($C_f = 0.025$, dashed and dot-dash curves) solutions are shown for $Q_1 = 0.3, 0.6, 0.9$ l s^{-1}.

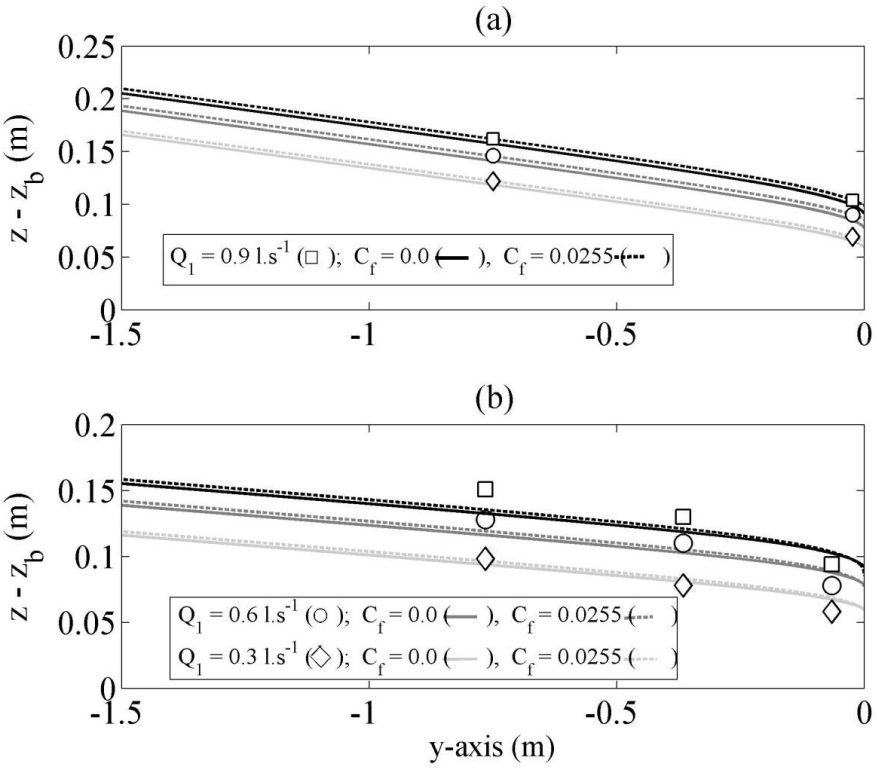

Figure 9 Density interface (ρ' = 0.5) elevation measurements (symbols) and inviscid (C_f = 0, solid curves) and frictional (C_f > 0.0255, dashed curves) flow predictions from the reduced gravity model for bed slopes of (a) ϕ = 3.6° and (b) ϕ = 1.7°, and volumetric flows Q_1 shown.

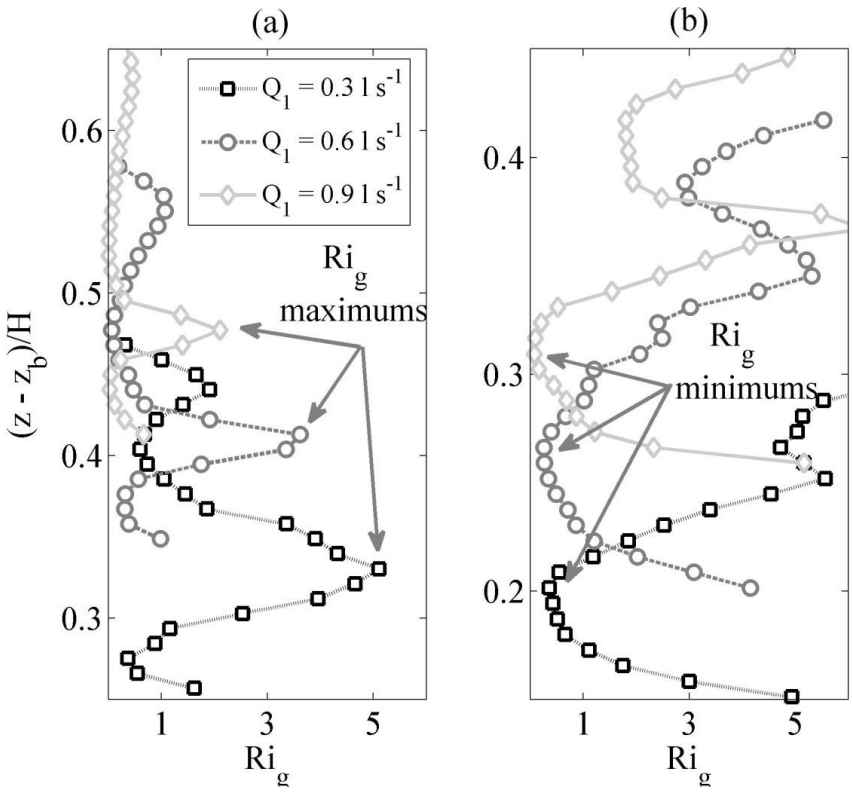

Figure 10 Gradient Richardson number Ri_g profiles for bed slopes of (a) $\phi = 3.6°$ and (b) $\phi = 1.7°$, obtained from time-averaged density and velocity profiles adjacent to sill section 6, for volumetric inflows Q_1 shown.

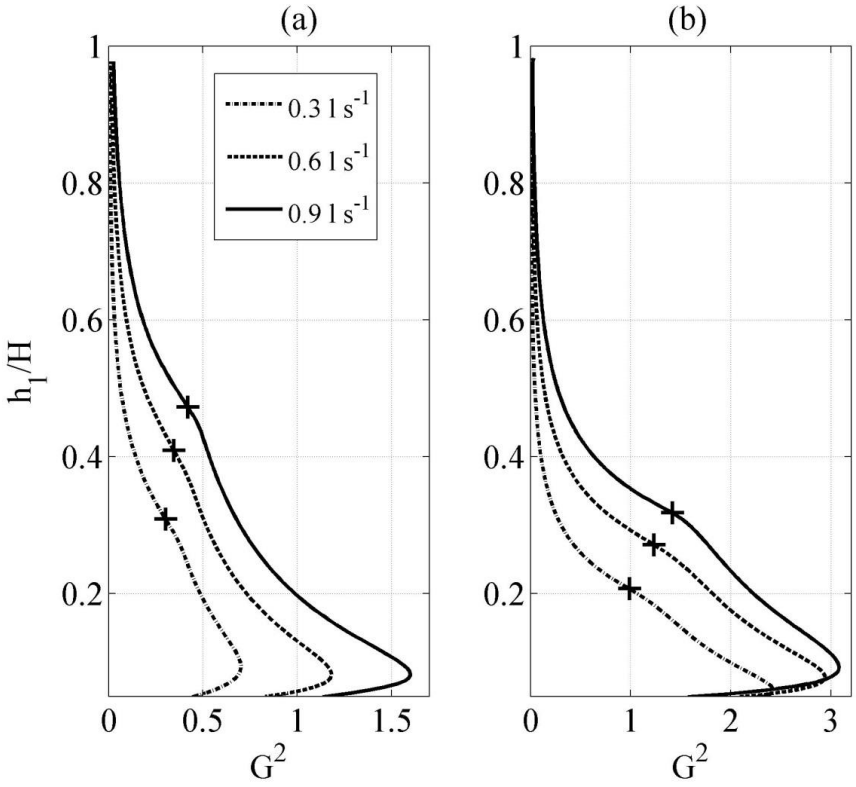

Figure 11 Predicted composite Froude number G^2 profiles [Eq. (8)] for bed slopes of (a) ϕ = 3.6° and (b) ϕ = 1.7°, calculated from cross-sectional average velocities $\bar{v}_0$ and $\bar{v}_1$ [Eq. (7)] and reduced gravity g' [Eq. (8)] profiles adjacent to sill section 6, for volumetric inflows Q_1 shown. The density excess ρ' = 0.5 interface positions are indicated by + symbols.

	Inlet section 1			Sill section 6				
Slope (ϕ)	Q_1 (l s^{-1})	g' (m s^{-2})	Π_1 (kg m^{-3})	Q_1 (l s^{-1})	g' (kg m^{-3})	Π_1 (kg m^{-3})	ΔQ_1 increase (%)	$\Delta\Pi_1$ error (%)
3.6°	0.3	0.123	0.303	0.302	0.114	0.304	0.67	0.39
	0.6	0.123	0.607	0.605	0.117	0.610	0.83	0.59
	0.9	0.123	0.910	0.907	0.118	0.915	0.78	0.61
1.7°	0.3	0.127	0.304	0.331	0.084	0.306	10.3	0.79
	0.6	0.127	0.608	0.654	0.084	0.614	9.00	0.90
	0.9	0.127	0.911	0.988	0.083	0.928	9.78	1.87

Table 1 Calculated volume fluxes Q_1, reduced gravitational accelerations g' and mass fluxes Π_1 at (i) inlet section 1 (i.e. source conditions) and (ii) the sill section. Corresponding ΔQ_1 and $\Delta\Pi_1$ values (section 1 $\rightarrow$ 6) are also estimated.

Slope (ϕ)	Q_1 (l s^{-1})	τ_i/ρ (cm^2 s^{-2})	$\nu.(dv/dz)$ (cm^2 s^{-2})	$w_{ei}.v_i$ (cm^2 s^{-2})	$\overline{v'w'}$ (cm^2 s^{-2})
ϕ = 3.6°	0.3	0.054	0.0158 (29.2%)	4.76×10^{-4} (0.9%)	0.0368 (68.1%)
	0.6	0.112	0.0230 (20.5%)	0.0013 (1.2%)	0.0877 (78.3%)
	0.9	0.149	0.0389 (26.1%)	0.0017 (1.1%)	0.1085 (72.8%)
ϕ = 1.7°	0.3	0.075	0.0289 (38.5%)	0.0166 (22.1%)	0.0296 (39.4%)
	0.6	0.108	0.0367 (34.0%)	0.0263 (24.3%)	0.0450 (41.7%)
	0.9	0.140	0.0601 (42.9%)	0.0417 (29.8%)	0.0382 (27.3%)

Table 2 Estimated total interfacial stress, represented by τ_i/ρ, and relative contributions due to viscous stress $\nu.(dv/dz)$, net entrainment effects $w_{ei}.v_i$ and turbulent Reynolds stress $\overline{v'w'}$.